Creation and characterization of free-standing cryogenic targets for laser-driven ion acceleration

Alexandra Tebartz , Stefan Bedacht, Markus Hesse , Sam Astbury, Rob Clarke, Alex Ortner, Gabriel Schaumann, Florian Wagner, David Neely and Markus Roth

Published version information

Citation: A Tebartz et al. "Creation and characterization of free-standing cryogenic targets for laser-driven ion acceleration." Review of Scientific Instruments, vol. 88, no. 9 (2017): 093512.

DOI: 10.1063/1.5001487

Review of Scientific Instruments

Creation and characterization of free-standing cryogenic targets for laser-driven ion acceleration

Cite as: Rev. Sci. Instrum. **88**, 093512 (2017); https://doi.org/10.1063/1.5001487
Submitted: 05 May 2017 . Accepted: 22 August 2017 . Published Online: 18 September 2017

Alexandra Tebartz, Stefan Bedacht, Markus Hesse, Sam Astbury, Rob Clarke, Alex Ortner, Gabriel Schaumann, Florian Wagner, David Neely, and Markus Roth

REVIEW OF SCIENTIFIC INSTRUMENTS **88**, 093512 (2017)

Creation and characterization of free-standing cryogenic targets for laser-driven ion acceleration

Alexandra Tebartz,[1,a)] Stefan Bedacht,[1] Markus Hesse,[1] Sam Astbury,[2] Rob Clarke,[2] Alex Ortner,[1] Gabriel Schaumann,[1] Florian Wagner,[3] David Neely,[2] and Markus Roth[1]
[1]*Institut für Kernphysik, Technische Universität Darmstadt, Schloßgartenstr. 9, 64289 Darmstadt, Germany*
[2]*Central Laser Facility, Rutherford Appleton Laboratory, Harwell Oxford, Chilton, Didcot, Oxon OX11 0QX, United Kingdom*
[3]*GSI Helmholtzzentrum für Schwerionenforschung GmbH, Planckstr. 1, 64291 Darmstadt, Germany*

(Received 5 May 2017; accepted 22 August 2017; published online 18 September 2017)

A technique for the creation of free-standing cryogenic targets for laser-driven ion acceleration is presented, which allows us to create solid state targets consisting of initially gaseous materials. In particular, the use of deuterium and the methods for its preparation as a target material for laser-driven ion acceleration are discussed. Moving in the phase diagram through the liquid phase leads to the substance covering an aperture on a cooled copper frame where it is solidified through further cooling. An account of characterization techniques for target thickness is given, with a focus on deducing thickness values from distance values delivered by chromatic confocal sensors. *Published by AIP Publishing.* [http://dx.doi.org/10.1063/1.5001487]

I. INTRODUCTION

In the research of laser-matter interaction, a wide range of material sample (*target*) substances and types is used to achieve different effects or examine various phenomena. The target type described in this work is assessed within the framework of being used as targets for laser-driven ion acceleration, which has become available with the development of high power lasers with sub-picosecond pulses in the petawatt range. Several mechanisms for the laser-driven acceleration of ions have been described, beginning with *Target Normal Sheath Acceleration* (TNSA).[1,2]

The targets usually consist of a non-volatile solid under standard conditions because those are easy to handle and transport while also stable *in vacuo*. However, target materials which are gaseous under standard conditions can be solidified at very low temperature. As an added advantage, solidification makes the material available at high density, unlike gas jet targets. At the same time, freestanding cryogenic targets are debris-free, eradicating the danger of damaging sensitive optical equipment by flying shrapnel or coating optical surfaces with laser-evaporated solids.

Different approaches have been developed for creating cryogenic targets: gases or liquids can be sprayed onto a cold surface to create a target that is coated with cryogenic materials,[3,4] extrusion of solidified gas from a high pressure reservoir,[5,6] and a droplet jet.[7] The cryogenic targets discussed in this paper were formed using the condensation method, where a cooled copper frame with an aperture for target formation is surrounded with gaseous deuterium. Its pressure and temperature are then manipulated to create a freestanding target.

II. COOLING UNIT

As cryogenic targets quickly evaporate without cooling, they cannot be transported and need to be produced and characterized *in situ*. Thus, a cooled setup is needed, realized by a closed circuit helium cooling unit made by SUMITOMO Cryogenics (RDK-415D, employing a modified Gifford-McMahon process) with a cooling power of 1.5 W at a base temperature of 4.2 K. In cooperation with Rutherford Appleton Laboratory, UK, usage of a pulse tube cryocooler[8] (SUMITOMO Cryogenics RP-082B) with a cooling power of 1.0 W at a base temperature of 4.2 K was also available. Both units are equipped for the attachment of actively cooled heat shielding to lower the amount of thermal radiation from the room temperature surroundings.

A cooling unit alone is not sufficient to produce cryogenic targets, as free navigation in the phase diagram is needed (see Sec. IV). The cooling process can only be operated in a binary fashion as the cooling power cannot be regulated, so closed loop temperature control is achieved with resistive heater cartridges, with power of up to 100 W, and temperature sensors. Gas pressure control is gained by enclosing the target frame in a motorized growth chamber. This allows us to reach high gas pressure without compromising the chamber vacuum. Please refer to Fig. 1 for a graphic representation of the setup for target creation that is attached to the cooling unit.

The Gifford-McMahon cooling unit provides a higher cooling power than the pulse tube cooler. This means that a higher amount of heat load can be compensated, which in correspondence allows us to use less radiation shielding, thus freeing up space for diagnostics close to the target. However, the Gifford-McMahon process relies on moving parts and thus produces vibrations,[9] so the cooling unit oscillates with a frequency of 1 Hz. Oscillation is almost completely along a one-dimensional axis whose orientation slowly rotates in

a)Author to whom correspondence should be addressed: atebartz@ikp.tu-darmstadt.de

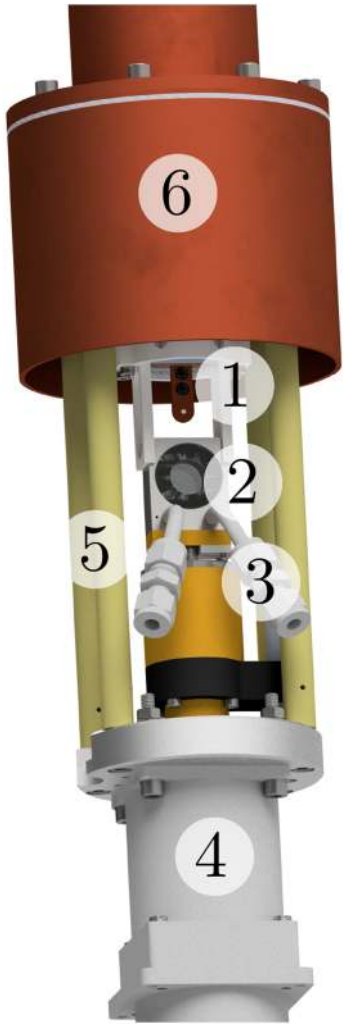

FIG. 1. This rendering shows the setup attached to the SUMITOMO RDK-415D cooling unit at TU Darmstadt as a 3D model. The exchangeable copper target frame (1) can be surrounded by a small movable growth chamber (with sapphire glass windows) of a few cubic centimeters volume (2) into which gas is supplied via connectors (3) (tubing omitted for clarity). The chamber is vertically movable so the target can be exposed for characterization or laser interaction. To reduce thermal coupling between the motor (4) and the cooling unit, fibreglass resin posts (5) are used as structural elements. Thus, less cooling power is wasted to cool down the motor and its housing. The comparatively high power of the cooling unit allows us to use minimal (cooled) heat shielding (6) (copper) which frees up a large solid angle for placement of diagnostics. Temperature sensors and heater capsules are inserted in the copper block [hidden behind heat shielding (6)] connecting the motorized mechanics and the cooling unit itself.

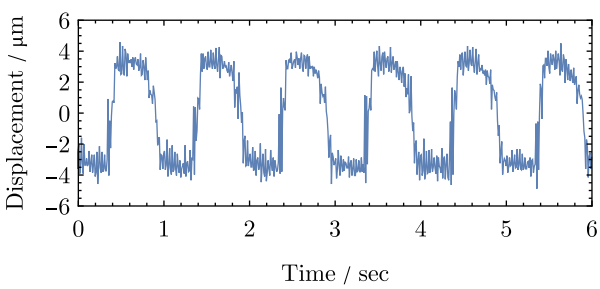

FIG. 2. Horizontal displacement of the cold head over time. The Gifford-McMahon process produces mechanical oscillations, so the cooling unit vibrates with a frequency of 1 Hz and a horizontal amplitude of approximately 4 μm.

space. The oscillation pattern and amplitude are displayed in Fig. 2.

III. TARGET MATERIAL

Pure hydrogen is a sought-after target material as it is the only pure proton source. Protons as the lightest ions are unique in their charge-to-mass ratio of one elementary charge per one nucleon mass, no other ion has a higher ratio. This can have an advantageous effect concerning the achievable kinetic energy in ion acceleration processes. Some models and simulations for laser-driven ion acceleration mechanisms predict the highest ion energies per nucleon for the highest charge-to-mass ratio, and thus protons.[10–12] Some of these even indicate that the presence of heavier nuclei lessens the efficiency of the acceleration of lighter ions, thus making a pure hydrogen target the most desirable.

However, there can be several advantages in the choice of the hydrogen isotope deuterium: Deuterium ions are discernible from hydrogen ions by charge-to-mass ratio, which makes them distinguishable in ion spectrometers such as Thomson parabolas.[13] This enables discrimination between ions that stem from the actual target material and ions from contamination layers that the target collects from residual water in the vacuum chamber or other contamination sources. Knowing the conditions under which a contamination-free ion beam can be realized is important for applications that require pure ion beams of a certain species.

In addition, the triple point temperature of deuterium (18.7 K) is higher than that of hydrogen (13.9 K)[14] (see also Fig. 6), which allows more leeway with the cooling power or heat bridges to the setup. Heat bridges cannot be avoided due to the addition of gas inlet tubing and heater cartridge power cables, both of which conduct heat directly.

Deuterium ions are preferable for applications like neutron beam generation:[15] A deuteron beam is directed onto a converter material[16] such as beryllium or lithium[17] from which neutrons are emitted via nuclear reactions. The so-called *deuteron breakup* produces a strong forward component in the neutron emission so that a directed neutron beam is possible.[17,18]

IV. TARGET CREATION

This section describes the process of target creation, starting with the target frame as the basic element of the setup. There are a multitude of different possible target geometries and substrates for cryogenic target growth: A two-dimensional copper foil with a serrated aperture aiding liquid saturation is employed at Rutherford Appleton Laboratory.[8] At TU Darmstadt, a three-dimensional design is used, which diverts the flow of liquid towards the aperture. The two designs are shown in Fig. 3 with details and dimensions in Figs. 4 and 5. The frame material was chosen to be copper for its high heat conductivity at low temperatures.

As the target frame gets deformed during laser-target interaction, it needs to be replaced every time. This entails warming up the setup to be able to vent and open the vacuum

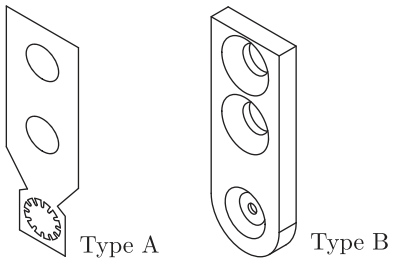

FIG. 3. Target frame designs: type A: a flat copper foil (25 μm) with a 3 mm serrated aperture; type B: a thick copper plate (2 mm) with a recessed aperture of 1 mm.

chamber and subsequently evacuate and cool again. The procedure totals to a cycle time of 3 h which is longer than the typical cycle time of contemporary high power lasers (90 min for the laser system PHELIX at GSI Helmholtzzentrum für Schwerionenforschung, Germany). A procedure and a setup for automated target frame exchange were developed and thermally simulated but have yet to be realized as a prototype.[19,20]

To achieve a freestanding target, the state of the material in the phase diagram is changed from gaseous to solid via the liquid phase, as the liquid is able to cover apertures in a target frame. Figure 6 illustrates that a pressure above the triple point needs to be reached to enter the liquid phase. Injecting deuterium gas into the entire vacuum chamber to a pressure of several hundred millibars should be avoided to prevent damaging the vacuum pumps via the sudden pressure increase and to prohibit massively increased heat conduction between cooled and uncooled parts and condensation onto every cold surface. Thus, a small vacuum-tight growth chamber [see Fig. 1 part (2)] of a few cubic centimeters volume is placed around the target frame and gas is let in.

We successfully created solid targets via this method from hydrogen, deuterium, and methane.

After target creation, the growth chamber is mechanically lowered to enable access for the laser beam for laser-target-interaction. We found that, while a base temperature just below the triple point is sufficient to solidify the material, removal of the growth chamber leads to a sudden increase in temperature (see Fig. 7) which is quickly rectified by the cooling mechanism, but a large temperature spike could cause the target to sublimate.

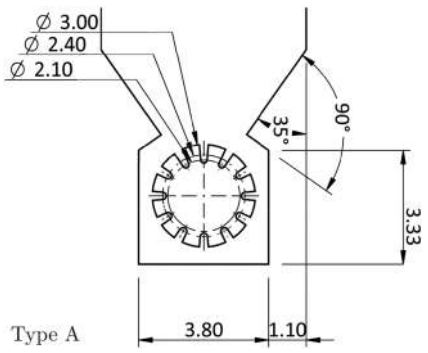

FIG. 4. Details and dimensions (in millimeters) of the flat foil target frame design with serrated aperture in top view.

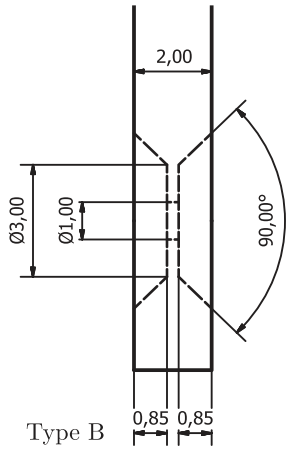

FIG. 5. Cross section of the three-dimensional target frame design. Dimensions are given in millimeters.

We suspect that the sudden temperature spike stems from solid materials deposited onto the surface of the cold growth chamber. Once the growth chamber is removed, the residual material quickly evaporates due to the removal of the cooling source which warms up the target through heat conduction and convection. If the temperature rises above the triple point, the target evaporates.

The hypothesis of a solid material evaporating upon growth chamber removal is supported by the fact that the temperature spike is smaller when the setup is placed in a larger vacuum chamber with higher pump power, as illustrated by

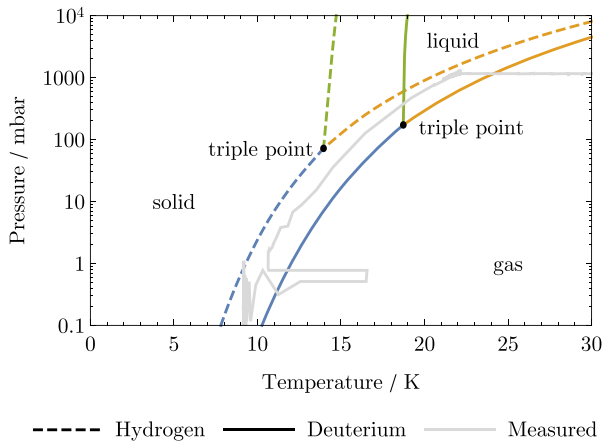

FIG. 6. The phase diagram [data from the work of Souers[14]] for hydrogen (dashed lines) and deuterium (solid lines) shows the difference in triple points for the two gases, illustrating that a cryogenic deuterium target can be generated at higher temperature (see Sec. III). The diagram also visualizes that a path from the gaseous phase via liquid to solid requires pressures above the triple point. Actual data from a target creation process with deuterium gas are inserted here in gray. After inserting gas, the setup is cooled below the triple point. The path is expected to run along the sublimation line as remaining gas in the growth chamber resublimates. The graph exhibits an offset towards a lower temperature compared to the expectation, which likely arises from the placement of the temperature sensors as their location is in a large thermal mass and protected by the heat shield, which is not the case for the target frame itself. In non-equilibrium situations like the cooldown process presented here, the temperature sensor surroundings cannot follow the target temperature in real time. The irregularity in temperature after cooldown and pressure reduction is discussed in Sec. IV and Fig. 7.

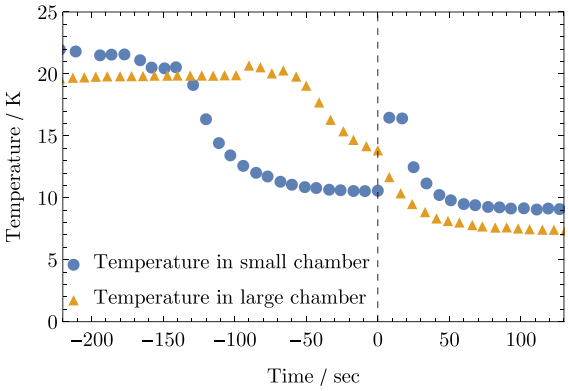

FIG. 7. Lowering the growth chamber after the creation of a solid target leads to a sudden temperature spike. The temperature spike disappears when the setup is placed in a larger vacuum chamber. The data were arranged such that the removal of the growth chamber happens at time 0 s.

the data in Fig. 7 which juxtaposes the temperature evolution during the process of growth chamber removal in a small vacuum chamber (approximately 0.3 m^3) and a large vacuum chamber (approximately 2 m^3). With the setup placed in the large vacuum chamber, the spike disappears or becomes small enough not to be apparent. One possible reason for a small spike not being visible in the data is that it could be corrected by the cooling in a very short time. Another reason is the location of the temperature sensor which is placed not exactly on the target frame but in a larger thermal mass, thus leading to damping and delay in non-equilibrium situations.

As a consequence of the possibility of target destruction due to the aforementioned temperature spike in a small vacuum chamber, special care must be taken to ensure sufficient cooling power and shielding against thermal radiation from the surroundings to reach a base temperature low enough that the temperature stays below the triple point while compensating the temperature spike upon growth chamber removal.

Note that temperature after growth chamber removal is lower than before for both vacuum chamber sizes. This is caused by the fact that removing the growth chamber lessens the thermal coupling to the motor unit, thus decreasing the heat load on the cooling unit.

V. TARGET CHARACTERIZATION

Since cryogenic targets are not transportable and have to be manufactured *in situ*, characterization is more difficult compared to conventional solid state targets. Two different target thickness measurement techniques are presented here, along with a camera setup for overview.

A. Frontview camera

A frontview camera permits the qualitative monitoring of ice formation to determine if there is liquid flowing or if the material has solidified already (see Fig. 8). The light emitted from the chromatic-confocal sensor (see Sec. V C) on the other side serves as a backlighter in this situation.

Once the process of target creation is sufficiently controllable without the need of a visual overview, the camera can be replaced with a second chromatic-confocal sensor.

B. Sideview camera

This method is applicable for two-dimensional target frames when the ice forming on them is thicker than the foil itself. The ice can be monitored with a sideview camera and with calibration; by comparison with the image of a wire with known thickness, the ice thickness can be determined (Fig. 9). Yet, one dimension is lost due to the projection, so only the

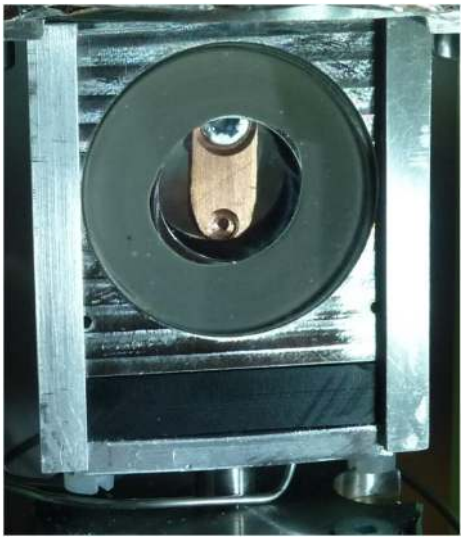

FIG. 8. The target frame is shown here as seen from the frontview camera (but with a larger field of view to illustrate the surroundings). With the glass windows (quartz in the picture, later changed to sapphire for greater durability), the target is visible even with the growth chamber closed.

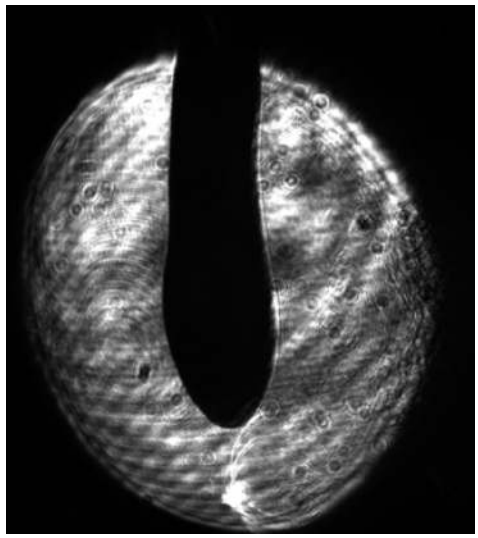

FIG. 9. A sideview camera produces shadowgraphy, which means any target thickness value can only be an upper boundary due to the projection. However, the picture reveals that the thickness is not necessarily constant in the vertical direction. The lateral dimension is lost due to the projection.

maximum thickness of the target at any given height is visible. Thus, thickness values obtained from a sideview camera can only be an upper boundary.

C. Chromatic-confocal sensor

White light focused with a highly dispersive lens system will yield images at different focal lengths, depending on wavelength. Chromatic confocal sensors utilize the variation of focal length to determine the distance to a reflective surface by analysis of the wavelength which forms a focused image. We used sensors by Precitec with a large measuring range of 2 mm (chromatic-confocal sensor head 5 005 126).[21] As the sensors are fairly large (33 mm diameter) and need to be close to the target with an operating distance of 14 mm, the cooling power needs to be high enough to allow such a large opening in thermal radiation shielding for sensor access. The reflectivity of frozen hydrogen/deuterium is low, so precise alignment is important.

As the measuring spot diameter is only 12 μm,[21] a two-dimensional profile can be created by scanning the target surface with motorized stages.

A single sensor can measure the distance, so to obtain thickness values, the geometry of the setup can be utilized (see Fig. 10 for a schematic illustration of the method). In this case, we measure the distance to the target frame itself (d_1) (without ice) and, assuming a symmetrical target and not moving the sensor along the target normal, the ice thickness is calculated from the known target frame thickness d_{frame} and the distance measured once the ice is in place (d_2). To improve the accuracy of this method, we characterized all target frames beforehand so their deviations from the manufacturing specifications were known

$$d_{\text{target}} = d_{\text{frame}} + 2 \times (d_1 - d_2). \tag{1}$$

As both d_1 and d_2 are superposed by the oscillation of the cooling unit (see Sec. II), a temporal average that smoothens the vibrations should be used in Eq. (1).

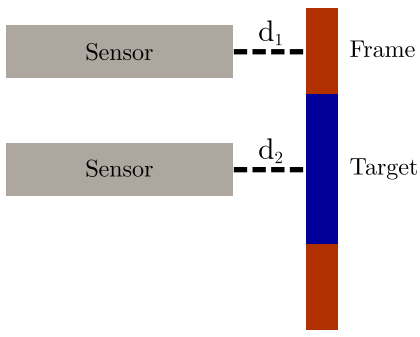

FIG. 10. Thickness values can be obtained under the assumption of a symmetric target by the difference in distance between the sensor and the target frame and the ice target, respectively. In addition, knowledge of the target frame thickness is necessary to obtain a thickness value. It should be noted that the sensor yields distance values (d_1, d_2) that are relative to the base point of its measuring range so that *distance* more accurately refers to the distance between the base point of the measuring range and the object. The resulting thickness values are not affected, so we refer to the *distance* in the schematic for simplicity.

D. Two chromatic-confocal sensors

With two chromatic confocal sensors from either side of the target, the assumption of a symmetric target is not necessary. Each sensor yields a distance value which requires a reference to convert it to a target thickness. Ceramic reference plates are available for calibration to link the sensor position to a target thickness. See Fig. 11 for a schematic illustration of the method. The distance values d_a and d_b from the sensors and the known thickness of the reference plate $d_{\text{reference}}$ add up to a total distance d_{total} that is constant for a fixed sensor position. With the reference plate swapped for the target, the target thickness can be determined using the constancy of d_{total}. Furthermore it should be noted that the oscillations in the distance values from the cooling unit vibration cancel each other out in the resulting thickness value,

$$d_a + d_{\text{reference}} + d_b = d_{\text{total}} = \text{const.}, \tag{2}$$

$$d_{a2} + d_{\text{target}} + d_{b2} = d_{\text{total}}, \tag{3}$$

$$d_{\text{target}} = d_{\text{total}} - d_{a2} - d_{b2}. \tag{4}$$

This method relies on a reference plate inside the target chamber which requires space and needs to be protected from the possibility of debris due to a possibly misaligned laser striking the target frame during the time of laser-matter interaction. In addition, as the reference plate cannot be in the same place as the target frame, a two-step process needs to be implemented. Either the plate itself needs to be motorized or the sensors have to be moved to the reference plate and then to the target with the crucial requirement that the distance d_{total} stays either unchanged during the movement or is restored at the target. Motorized stages with sub-micrometer accuracy are commercially available.

It needs to be considered that, as the reflectivity of the ice surface is low, either sensor can receive light from its partner on the other side of the target, depending on target transmissivity (and thus thickness). This can obscure the actual distance information required for the thickness calculation. To avoid

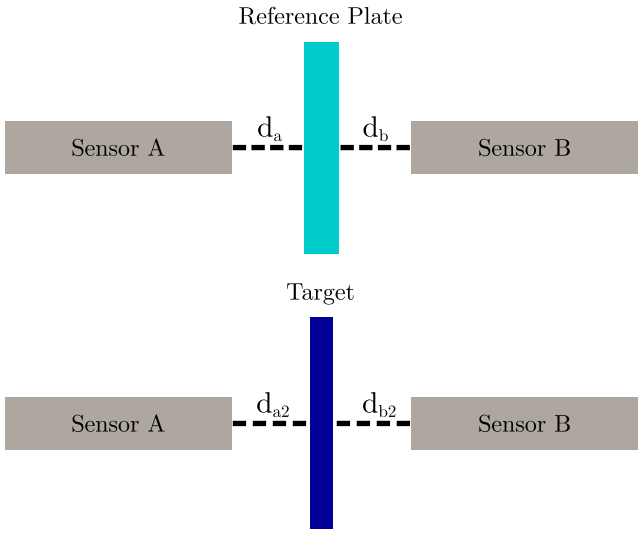

FIG. 11. A reference plate between the sensors yields a calibration that links sensor position to target thickness, provided the distance between the sensors stays constant.

this, we propose motorized covers for the sensors which can be employed to ensure that a sensor only receives the reflection of its own light.

The sensors have to be mounted on a motorized base because they need to be moved to clear the way for the laser before laser-target interaction. Programming a scanning pattern for the motorized bases can be employed to gain a surface map for the target. Thus, information about the surface could be obtained but it has yet to be done.

VI. LONGEVITY AND TEMPORAL THICKNESS DEVELOPMENT

Target longevity is an issue that needs to be considered when taking into account that the time between target creation and laser-target interaction cannot be arbitrarily short, as the removal of the growth chamber, the characterization process, and the removal of the sensor from the laser path need time. The survival of the target during the removal of the growth chamber is addressed in Sec. IV and Fig. 7. However, after complete removal of the growth chamber, the target is exposed to thermal radiation from surrounding equipment and the walls of the vacuum chamber, which are at room temperature. The effects of thermal radiation on target survivability were studied; Fig. 12 presents the thickness of a deuterium target over time.

The reference frame for target lifetime is given by the actions that need to be taken between target creation and successful laser-target interaction: The time needed for removal of the growth chamber (a few seconds), the characterization process (a few seconds to tens of seconds, depending on the desired accuracy for the determination of the sublimation rate), and the removal of the sensor from the laser path (a few tens of seconds). As the change in thickness over time is very small, the target lifetime is amply sufficient for the time needed for laser shot preparation.

As the geometry of the target does not change much during the slow sublimation, we expect a constant sublimation rate and thus a linear thickness evolution. The temporal thickness development from Fig. 12 is fitted with polynomial functions. To assess the linearity of the thickness development, we compare a linear function d_{target1} to a function of second order d_{target2} to allow for an accelerated sublimation rate

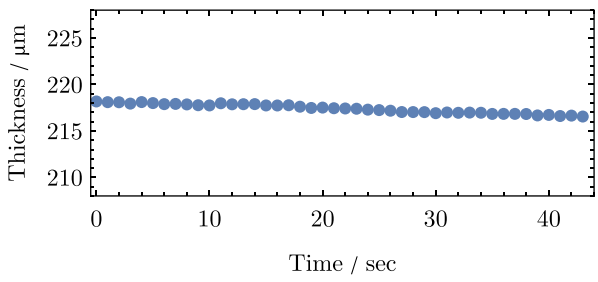

FIG. 12. The time-dependent thickness of a deuterium ice target is measured with the single confocal sensor technique presented in Sec. V C. The vibrations of the cooling unit are smoothed out here by averaging over one vibration cycle of the cooling unit (1 s). The sublimation rate is very small compared to the timeline of events between target creation and laser-laser interaction, so target survival is not an issue.

TABLE I. Difference between the two fit functions for target thickness at several extrapolated points of time.

t/s	$\Delta d/\mu$m
60	0.2
90	0.8
120	1.7

$$d_{\text{target1}}(t) = a \times t + b, \tag{5}$$

$$d_{\text{target2}}(t) = c \times t^2 + d \times t + e. \tag{6}$$

The following fit parameters are calculated with gnuplot:[22]

$$a = -3.83 \times 10^{-2}\ \mu\text{m/s}, \tag{7}$$

$$c = -1.74 \times 10^{-4}\ \mu\text{m/s}^2, \tag{8}$$

$$d = -3.09 \times 10^{-2}\ \mu\text{m/s}. \tag{9}$$

The linear sublimation rates a and d from both models are very similar, and the quadratic term c is very small. We compare the extrapolation that the two models yield via their difference $\Delta d = d_{\text{target1}}(t) - d_{\text{target2}}(t)$ at several points of time in Table I.

We conclude from the small sublimation rate and the agreement of the linear and quadratic fit model that determination of target thickness at the time of laser-target-interaction by linear extrapolation is valid if the time span between the characterization and the laser interaction is less than 2 min. This is an achievable threshold.

We have not yet succeeded in producing targets with a lower thickness than the 200 μm range (see Fig. 12), which is high compared to the target thickness usually employed for TNSA-experiments. We anticipate to be able to produce thinner targets with a growth chamber of smaller dimensions, so less material is needed to reach the required pressure for the liquid phase, and a more precise mass flow controller.

VII. CONCLUSIONS

We successfully created freestanding cryogenic hydrogen, deuterium, and methane targets in a copper frame by moving through the phase diagram via the liquid phase. The necessary pressure for the phase change is achieved by introducing gas into a small growth chamber which surrounds the target frame and is removed after the target creation process to allow laser interaction. The process is also applicable to other gaseous materials to make them available as targets at solid density.

Characterization methods by camera and by chromatic-confocal sensor are presented in this work. Cameras provide a direct overview over target formation and can also be used to quantify the target thickness when placed with a view axis along the target plane. Chromatic-confocal sensors placed in the target normal (on one or both sides of the target) measure the distance to the target surface. Utilizing the geometry of the setup or a separate reference plate yields the target thickness.

Once the growth chamber is removed, the target is exposed to the vacuum and the black body radiation from the

room-temperature surroundings. The sublimation rate is very low, and the target lifetime is very long compared to the timeline of events between target creation and laser interaction, so target survival is not an issue.

We analyzed the temporal development of the target thickness and compared it to a linear and quadratic model with regard to the extrapolation of temporal evolution. We found that a linear model is valid for extrapolation of a target thickness for a range of around 2 min, which allows enough time for the characterization process and the removal of the sensor from the laser path before laser interaction.

ACKNOWLEDGMENTS

We wish to acknowledge the support of the teams at the Detector- and Target Laboratory at TU Darmstadt and the Target Fabrication Group at Rutherford Appleton Laboratory, including the resident engineering teams.

We also wish to express our sincere thanks for funding by Deutsche Forschungsgemeinschaft (DFG) (Project No. RO 2515/61, DFG), Laserlab Europe (Grant No. 284464), and EPSRC (Grant No. EP/K022415/1, Professor Marco Borghesi).

Data associated with research in this paper can be accessed via http://dx.doi.org/10.5286/edata/704.

[1]R. A. Snavely, M. H. Key, S. P. Hatchett, T. E. Cowan, M. Roth, T. W. Phillips, M. A. Stoyer, E. A. Henry, T. C. Sangster, M. S. Singh, S. C. Wilks, A. Mackinnon, A. Offenberger, D. M. Pennington, K. Yasuike, A. B. Langdon, B. F. Lasinski, J. Johnson, M. D. Perry, and E. M. Campbell, Phys. Rev. Lett. **85**, 2945 (2000).

[2]S. C. Wilks, A. B. Langdon, T. E. Cowan, M. Roth, M. Singh, S. Hatchett, M. H. Key, D. Pennington, A. MacKinnon, and R. A. Snavely, Phys. Plasmas **8**, 542 (2001).

[3]J. T. Morrison, M. Storm, E. Chowdhury, K. U. Akli, S. Feldman, C. Willis, R. L. Daskalova, T. Growden, P. Berger, T. Ditmire, L. Van Woerkom, and R. R. Freeman, Phys. Plasmas **19**, 030707 (2012).

[4]A. G. Krygier, J. T. Morrison, S. Kar, H. Ahmed, A. Alejo, R. Clarke, J. Fuchs, A. Green, D. Jung, A. Kleinschmidt, Z. Najmudin, H. Nakamura, P. Norreys, M. Notley, M. Oliver, M. Roth, L. Vassura, M. Zepf, M. Borghesi, and R. R. Freeman, Phys. Plasmas **22**, 053102 (2015).

[5]S. Garcia, D. Chatain, and J. P. Perion, Laser Part. Beams **32**, 569 (2014).

[6]D. Margarone, A. Velyhan, J. Dostal, J. Ullschmied, J. P. Perin, D. Chatain, S. Garcia, P. Bonnay, T. Pisarczyk, R. Dudzak, M. Rosinski, J. Krasa, L. Giuffrida, J. Prokupek, V. Scuderi, J. Psikal, M. Kucharik, M. D. Marco, J. Cikhardt, E. Krousky, Z. Kalinowska, T. Chodukowski, G. A. P. Cirrone, and G. Korn, Phys. Rev. X **6**, 041030 (2016).

[7]M. Gauthier, J. B. Kim, C. B. Curry, B. Aurand, E. J. Gamboa, S. Göde, C. Goyon, A. Hazi, S. Kerr, A. Pak, A. Propp, B. Ramakrishna, J. Ruby, O. Willi, G. J. Williams, C. Rödel, and S. H. Glenzer, Rev. Sci. Instrum. **87**, 11D827 (2016).

[8]S. Astbury, S. Bedacht, P. Brummitt, D. Carroll, R. Clarke, S. Crisp, C. Hernandez-Gomez, P. Holligan, S. Hook, J. S. Merchan, D. Neely, A. Ortner, D. Rathbone, P. Rice, G. Schaumann, C. Spindloe, S. Spurdle, A. Tebartz, S. Tomlinson, F. Wagner, M. Borghesi, M. Roth, and M. Tolley, J. Phys.: Conf. Ser. **713**, 012006 (2016).

[9]A. T. A. M. de Waele, J. Low Temp. Phys. **164**, 179 (2011).

[10]J. Schreiber, F. Bell, F. Grüner, U. Schramm, M. Geissler, M. Schnürer, S. Ter-Avetisyan, B. M. Hegelich, J. Cobble, E. Brambrink, J. Fuchs, P. Audebert, and D. Habs, Phys. Rev. Lett. **97**, 045005 (2006).

[11]F.-C. Wang, Chin. Phys. B **22**, 124102 (2013).

[12]B. M. Hegelich, I. Pomerantz, L. Yin, H. C. Wu, D. Jung, B. J. Albright, D. C. Gautier, S. Letzring, S. Palaniyappan, R. Shah, K. Allinger, R. Hörlein, J. Schreiber, D. Habs, J. Blakeney, G. Dyer, L. Fuller, E. Gaul, E. McCary, A. R. Meadows, C. Wang, T. Ditmire, and J. C. Fernandez, New J. Phys. **15**, 085015 (2013).

[13]J. J. Thomson, Proc. R. Soc. A **89**, 752 (1913).

[14]P. C. Souers, *Hydrogen Properties for Fusion Energy* (University of California Press, Berkeley, Los Angeles, London, 1986).

[15]A. Alejo, A. G. Krygier, H. Ahmed, J. T. Morrison, R. J. Clarke, J. Fuchs, A. Green, J. S. Green, D. Jung, A. Kleinschmidt, Z. Najmudin, H. Nakamura, P. Norreys, M. Notley, M. Oliver, M. Roth, L. Vassura, M. Zepf, M. Borghesi, R. R. Freeman, and S. Kar, Plasma Phys. Controlled Fusion **59**, 064004 (2017).

[16]S. Fritzler, Z. Najmudin, V. Malka, K. Krushelnick, C. Marle, B. Walton, M. S. Wei, R. J. Clarke, and A. E. Dangor, Phys. Rev. Lett. **89**, 165004 (2002).

[17]T. Ye, Y. Watanabe, and K. Ogata, Phys. Rev. C **80**, 014604 (2009).

[18]E. C. May, B. L. Cohen, and T. M. O'Keefe, Phys. Rev. **164**, 1253 (1967).

[19]M. Hesse, "Erhöhung der repetitionsrate bei experimenten zur laser-ionenbeschleunigung mit kryogenen targets," Master's thesis, Technische Universität Darmstadt, 2016.

[20]M. Hesse, "Shortened turnaround time of cryogenic targets for laser-driven ion acceleration," in 6th Target Fabrication Workshop, Greenwich, UK, 2017.

[21]See http://www.precitec.de/en/products/optical-measuring-technology/chromatic-confocal-sensors/chrocodile-s-se/ for "Precitec Group: Overview–Optical Probes."

[22]See http://www.gnuplot.info/ for "Gnuplot Version 5.0."